

A comprehensive study of pumice formation and dispersal: the Cretaio Tephra of Ischia (Italy)

G. Orsi^a, G. Gallo^a, G. Heiken^b, K. Wohletz^b, E. Yu^b and G. Bonani^c

^aDipartimento di Geofisica e Vulcanologia, University of Naples, Naples, Italy

^bLos Alamos National Laboratory, Los Alamos, NM, USA

^cInstitut für Mittelenergiephysik, ETH, Zurich, Switzerland

(Received August 14, 1991; revised and accepted March 4, 1992)

ABSTRACT

Orsi, G., Gallo, G., Heiken, G., Wohletz, K., Yu, E. and Bonani, G., 1992. A comprehensive study of pumice formation and dispersal: the Cretaio Tephra of Ischia (Italy). *J. Volcanol. Geotherm. Res.*, 53: 329–354.

The Cretaio Tephra is a small-volume ($<0.02 \text{ km}^3$) pumice deposit on the island of Ischia in Italy. It was erupted during historical time and is associated with a tuff ring-dome complex extruded along a N–S-trending normal fault system bordering the east side of the Mt. Epomeo resurgent block. ^{14}C ages of the deposit average 1860 a B.P., which is in agreement with the potsherds found in paleosols underlying and overlying the deposit. The eruption sequence consists of 7 members; most of these members are pumice fall deposits, one is an ash and pumice fallout and another is a surge bed. The tephra have a trachytic–phonolitic composition. All chemical characteristics, including major and trace elements, and Sr-isotope composition are homogeneous throughout the sequence. The vesicularity of pumice clasts does not show any systematic change; the erupted magma had the same amount of volatiles, the same flux and vesicle growth behavior throughout the eruption sequence. Grain-size analyses of 90 tephra samples, representative of all the members at variable distance from the supposed vent, have been processed using the Sequential Fragmentation/Transport theory in order to define the effects of eruptive fragmentation and subsequent transport on the particle sizes distribution. Four significant subpopulations have been identified and related to transport mechanisms.

Introduction

The purpose of this work is to apply a large variety of volcanological techniques to a small-volume pumice deposit; some of the techniques are traditional (grain size, mineralogical, chemical) and some new and untried (sequential fragmentation theory and image analysis techniques for vesicles). The deposit chosen for the study is the Cretaio Tephra, a pumice and ash deposit associated with the young (historical) trachytic dome and tuff ring complexes of the island of Ischia, Italy.

Ischia, a densely inhabited volcanic island, is part of the volcanic region of the Bay of Naples that also includes the island of Procida and the Phlegrean Fields (Fig. 1A). Its magmatic history during the last 55 ka has been subdivided in three main periods: (1) 55 to 33 ka; (2) 28 to 18 ka; and (3) 10 ka to 1302 AD, when the last eruption occurred at Arso volcano (Fig. 1C) (Chiesa et al., 1987; Civetta et al., 1991). The activity during the most recent period was on the eastern side of the island, where most of the eruptive vents are aligned N–S along tensile faults bordering the eastern edge of the Mt. Epomeo resurgent block (Orsi et al., 1991). A few of the youngest vents are located along an ENE–WSW-trending fault

Correspondence to: G. Orsi, Dipartimento di Geofisica e Vulcanologia, University of Naples, Largo S. Marcellino 10, 80138 Naples, Italy.

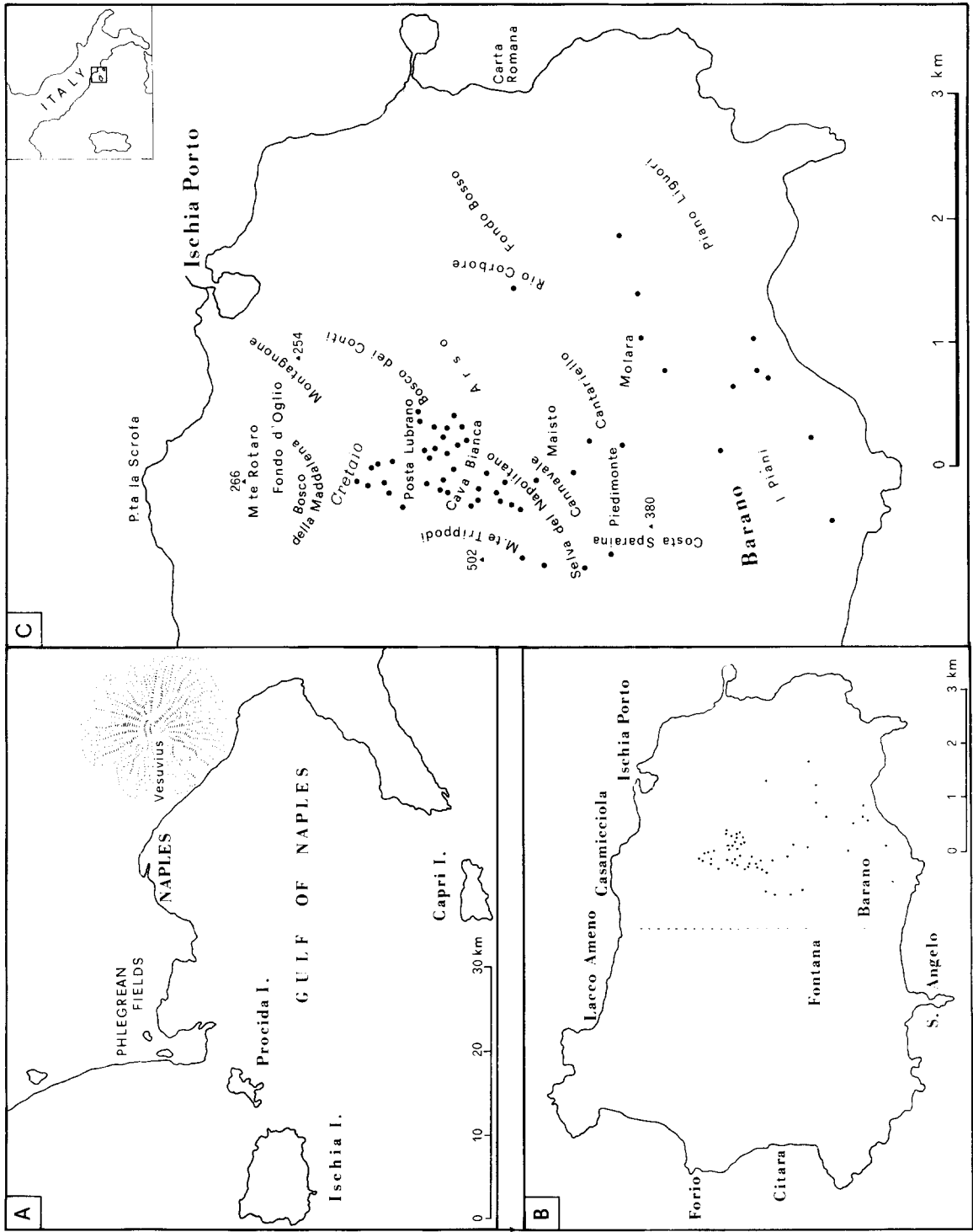


Fig. 1. (A) Location map of the island of Ischia, in the same volcanic province as the Phlegrean Fields, island of Procida, and Vesuvio. (B) Outline map of Ischia. Area to the right of the dotted line is the location of map C. (C) Eastern half of the island of Ischia, showing location of measured stratigraphic sections of the Cretatio Tephra (dots) and location of geographic features mentioned in the text.

system that crosses the southeastern corner of the island.

Volcanism during the youngest period of activity has been characterized by explosive eruptions and dome growth; many of the explosive eruptions were hydromagmatic. The beginning of the most recent period of activity was characterized by complex geochemical and isotopic trends and was contaminated by the eruption of magmas with less radiogenic Sr-isotope composition (≈ 0.70600) in respect to the last-erupted magma of the previous period of activity (≈ 0.70640) (Chiesa et al., 1987; Civetta et al., 1991).

A detailed reconstruction of the eruptive history of the most recent period of activity at Ischia is still lacking in the published literature. While studying these younger deposits, we decided to pick one of them for a detailed study. Selected for this study is a fallout deposit from one of the youngest eruptions; it was named the Cretaio Tephra, after exposures adjacent the Plain of Cretaio. In the recently published geological map of Ischia (Vezzoli, 1988) the rocks of this unit have been mapped, together with those of five other pyroclastic deposits separated by four paleosols (Orsi and Gallo, in prep.), as "pumiceous tephra" from craters now filled with trachytic domes (Selva del Napolitano, Piedimonte, Cannavale).

Stratigraphic position and age

The Cretaio Tephra (CT) is widespread over eastern Ischia. It does not crop out in the area between Punta la Scrofa, Arso and Carta Romana in the northeasternmost corner of the island (Figs. 1B and 1C), where it is covered by younger deposits.

The CT usually overlies a paleosol which developed on a variety of older deposits, including the Piano Liguori Formation (Rittmann and Gottini, 1980), the ash layers overlying the Posta Lubrano dome, scoria-fall beds of the

Molara edifice, the Cava Bianca Tephra, the pumice fallout overlying the Rio Corbore lavas, the stratigraphically highest of the five pyroclastic units with an intercalated landslide deposit cropping out at Monte Trippodi, and the southwesternmost lava dome of the Cantariello area. All the aforementioned pyroclastic deposits and the Cantariello dome have been described recently by Orsi and Gallo (in prep.) and Civetta et al. (1991). In some places (I Piani; Fig. 1C) the paleosol contains pottery of Roman age (G. Buchner, pers. commun., 1991).

In the area of Fondo Bosso (Fig. 1C) the CT is overlain by a paleosol, which is surmounted by the Bosco dei Conti Tephra fallout (BdC T; Orsi and Gallo, in prep.); this tephra bed also covers the CT in the area of Posta Lubrano and Bosco dei Conti (Fig. 1C), where the contact is marked by the presence of charred wood. Late Roman to mediaeval (G. Buchner, pers. commun., 1991) jar fragments have been found at Maisto in a thick paleosol overlying the CT. At Maisto and Cantariello (Fig. 1C) the CT is overlain by pyroclastic deposits of magmatic and hydromagmatic origin; Vezzoli (1988) has included these deposits, together with the CT, in the products of eight coeval pumice cones forming the Cantariello Volcanic Center; these are not pumice cones, but are lava domes covered by these pyroclastic deposits (Orsi and Gallo, in prep.). Landslide deposits, although widespread in the area, have never been found overlying the CT.

Humic acids extracted from two samples (OIS 200 and OIS 224 P) were dated. The middle of the calibrated age range is around 150 AD (Table 1), and is assumed as the age of the eruption. These dates are supported by the pieces of pottery collected in the paleosol underlying the CT; they have been identified as Roman (G. Buchner, pers. commun., 1991). However, they are made of a material used by poor people over a long period of time; it is not possible to define the precise century.

TABLE 1

¹⁴C age determinations

Lab. no.	Sample no.	AMS ¹⁴ C age (yrs BP)	δ ¹³ C (‰)	Calibration age (BC-AD)
ETH-4960	OIS 200	1,970 ± 70	-25.3 ± 1.3	BC 162-AD 207
ETH-6301	OIS 224P	1,750 ± 70	-26.1 ± 1.9	AD 114-AD 424

The eruption sequence

The Cretaio Tephra (CT) is a fallout deposit mostly composed of juvenile pumice and ash and lithic clasts. The juvenile components are mostly white with subordinate pinkish pumice, and minor greenish-gray slightly vesicular fragments. Lithic clasts are compositionally homogeneous throughout the entire unit, and the majority is composed of gray porphyritic trachytic lavas. Few black lava and rare subvolcanic clasts have been found. The CT overlies a well-developed soil, which covers underlying tephra deposits and lavas.

57 stratigraphic sections (Fig. 1C) have been measured, and the unit has been subdivided into 7 members designated A through G from base upward (Fig. 2A). Some of the members have been subdivided in layers according to textural and grain-size variations.

The Cretaio Tephra attains its maximum thickness of about 3 m in the area of Cretaio, and decreases southward. The thickness of each member varies in the same way, with some modification by erosion or post-depositional accumulation. In places the erosion is very deep and some of the highest members are absent.

Member A. This member occurs only in the area of Cretaio and reaches a maximum thickness of 53 cm. It is whitish gray in color and composed of ash- to lapilli-sized particles with scattered and rounded pumice clasts and 20% lithic clasts.

Member B. This member has been found in almost all the measured sections and attains a maximum thickness of 33 cm. It is massive and composed of pinkish pumice with subordinate

lithic clasts. Both juvenile and lithic clasts are angular. Fine ash is dispersed throughout the deposit.

Member C. This fallout member, whose thickest exposure is 130 cm, is present in all the measured sections. It has been subdivided into layers, each of which is composed of about the same percentage of white pumice fragments and gray lithic clasts, which are normally graded. The number of layers in the different sections varies from 6 to 2. The highest number has been measured in sections located in the area of Monte Trippodi (Fig. 1).

Member D. This fallout member is composed of greenish-gray vesicular juvenile fragments and lithic clasts. It consists of three massive layers, and the intermediate layer is the finest grained. The juvenile fragments, representing parts of broken pumice and/or bombs are less vesicular than the pumice fragments of the other members. The lithic clasts are smaller than a few millimeters.

Member E. This member has been found in all of the measured sections. It is subdivided into three parts, with the lower and upper parts composed of fine ash- to lapilli-sized particles with few small rounded pumices, while the middle layer is made up mostly of rounded pumice fragments in a fine matrix.

Member F. This fallout member is very similar to member C. It has been subdivided into four layers. Each layer is composed of pumice fragments and lithic clasts. Pumice fragments, accounting for 60% of the deposit, are angular and whitish-gray in color. Angular lithic clasts are abundant, and make up the remaining part of the deposit.

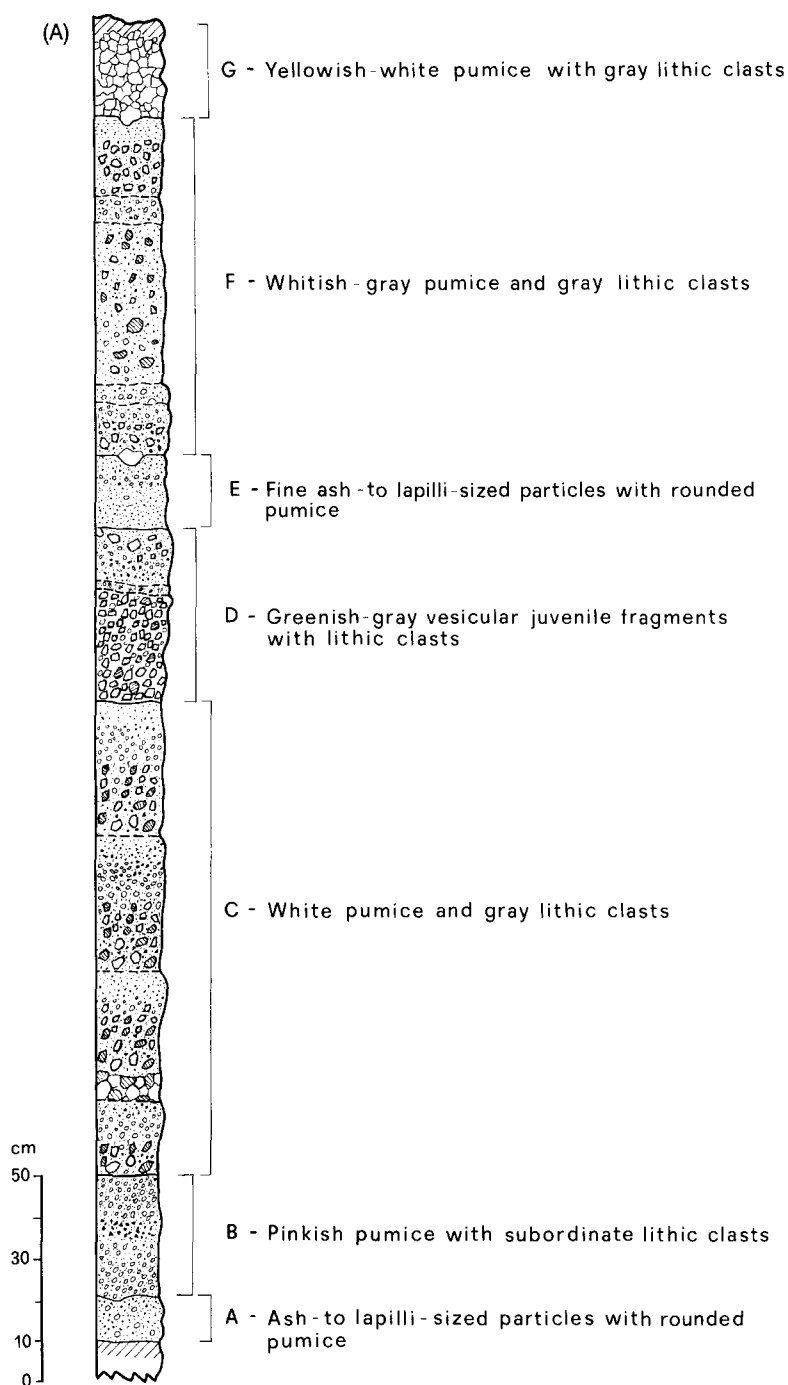


Fig. 2. (A) Stratigraphic section of the Cretaio Tephra, measured near the type locality (see Fig. 1). The Cretaio Tephra consists of seven discrete members, consisting of five pumice and ash fallout beds and two fine-grained surge deposits.

Member G. This fallout member only crops out in few sections in the western part of the island. It is composed of yellowish-white pum-

ice fragments and subordinate gray lava lithic clasts. In many of the measured sections this member has been eroded.

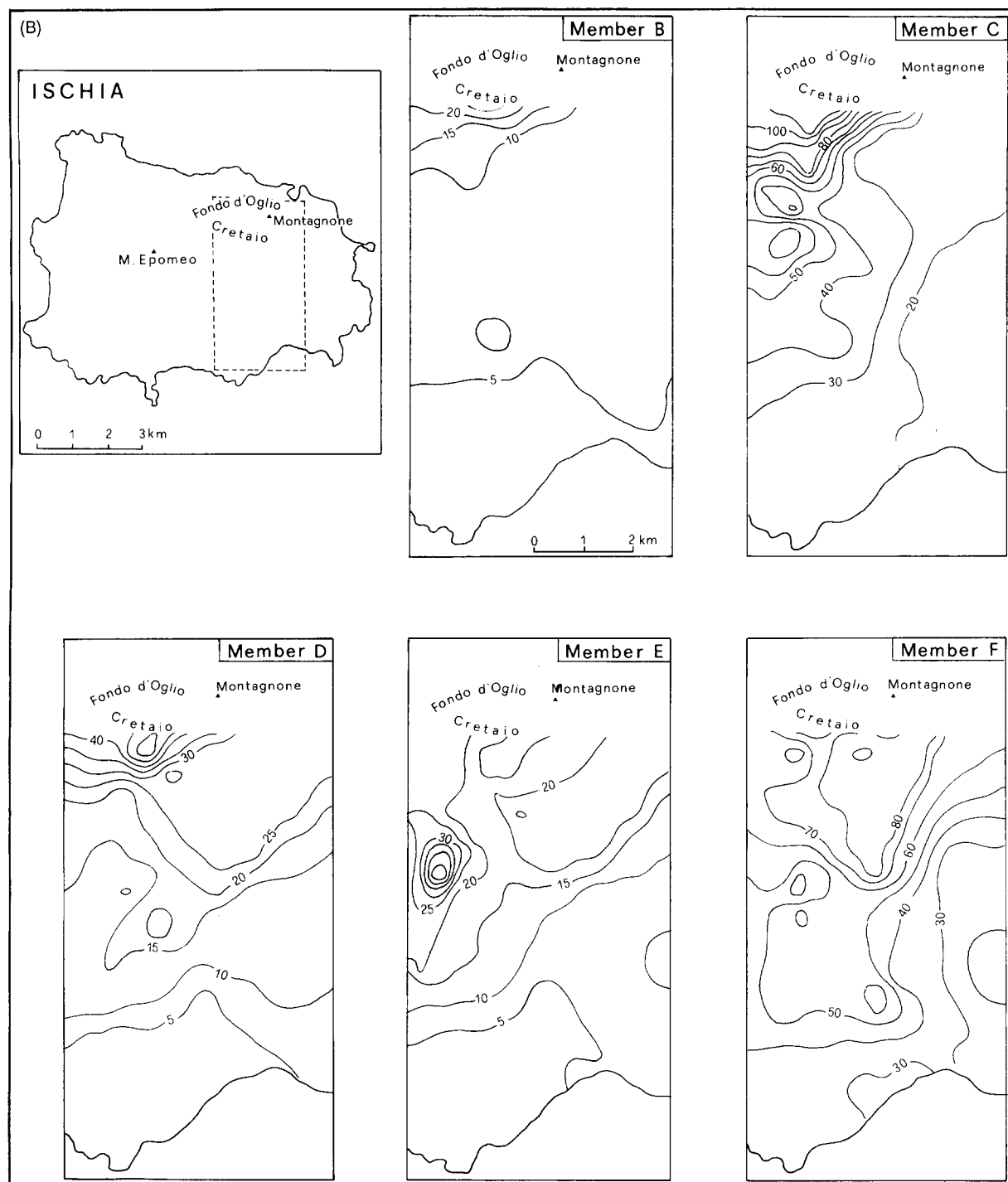


Fig. 2. (B) Thickness of each member of the Cretaio Tephra, in centimeters.

Location of the source of the Cretaio Tephra

A field survey has shown no evidence of an eruptive vent or an edifice that could be re-

lated to the eruption of the CT layers that are not correlatable. On the basis of areal distribution and thickness and maximum components variation we suggest that the eruptive

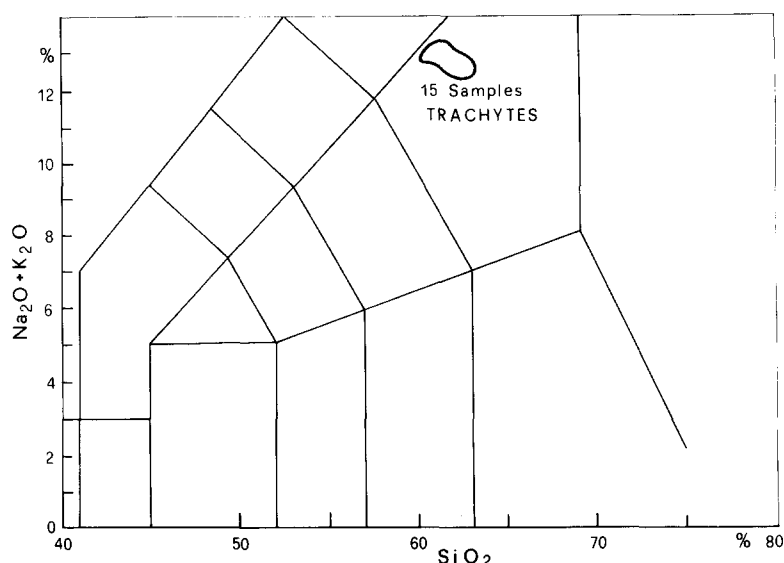


Fig. 3. TAS diagram for Cretaio Tephra samples.

vent for the CT was located in the area now occupied by the Bosco della Maddalena and Monte Rotaro volcanic edifices (Fig. 1C). The activity of these volcanoes is younger than the eruption of the CT. The CT disappears at the base of the Bosco della Maddalena edifice that is covered by the BdC T which overlies the CT. The BdC T is overlain by another pyroclastic unit (Bosco della Maddalena Tephra; Orsi and Gallo, in prep.) which is overlain by the Montagnone dome. The eruption that produced the CT must have built a pyroclastic cone, later destroyed by the activity of the Bosco della Maddalena volcanic edifice.

The thickness of the CT varies from 3 to 0.7 m over a distance of about 4 km. Variation of the thickness with distance from the supposed vent shows a decrease up to 2–3 km and then an increase and another decrease (Fig. 2B). The increases and decreases in total thickness beyond 2.4 km appear to have been caused by reworking, perhaps by sheetflow erosion of the pumice deposit from hills into the valley near Piedimonte and Pilastri. This interpretation applies equally to fall and surge deposits. The estimated volume of this deposit is $<0.02 \text{ km}^3$ DRE.

Mineralogy, geochemistry and isotope-geochemistry

Pumice samples representative of all the members and of some of the layers were collected in order to define the mineralogical assemblage, and chemical and Sr-isotope composition. The mineralogical assemblage is defined by K-feldspar, plagioclase and biotite with minor augite and scarce Fe–Ti oxides. Fifteen composite pumice samples were analyzed at the University of Milano by XRF in order to determine major and trace element concentrations with the exception of MgO, Na₂O, K₂O and MnO which were determined by AAS. The results of these analyses are reported in Table 2. In the TAS diagram (Fig. 3), the analyzed rocks fall on the line dividing the trachyte and phonolite fields. Major and trace element concentrations are homogeneous throughout the unit. The results of Sr-isotope determinations on whole-rock and K-feldspar separates of three samples collected at base, top and median part of the CT sequence, are reported in Table 3. The values shown by the K-feldspar separates are similar within the errors indicating that the magma was not af-

TABLE 2

Chemical data

Sample:	OIS200A	OIS200B	OIS200C1	OIS200C2	OIS200C3	OIS200C4	OIS200D1	OIS200D3	OIS200E	OIS200F1	OIS206F1	OIS206F3	OIS206G1	OIS206G4	OIS206G6
Member:	A	B	C(1)	C(2)	C(3)	C(4)	D(1)	D(3)	E	F(1)	F(1)	F(3)	G(1)	G(4)	G(6)
SiO ₂	61.72	61.64	62.06	62.07	61.93	61.96	61.90	62.16	62.56	61.83	61.53	61.89	61.64	61.84	61.83
TiO ₂	0.65	0.65	0.64	0.62	0.62	0.64	0.64	0.64	0.66	0.66	0.63	0.64	0.64	0.62	0.65
Al ₂ O ₃	18.88	18.77	18.64	18.88	18.84	18.92	18.81	18.84	16.68	18.93	18.57	18.74	18.79	18.67	18.82
FeO	3.06	3.04	3.00	3.01	2.90	3.04	3.00	3.01	3.41	2.99	2.94	2.94	2.94	2.97	2.97
MnO	0.15	0.15	0.17	0.15	0.15	0.16	0.15	0.14	0.17	0.16	0.15	0.14	0.15	0.15	0.14
MgO	0.66	0.73	0.59	0.51	0.61	0.51	0.64	0.72	0.71	0.67	0.80	0.72	0.72	0.60	0.60
CaO	1.61	1.66	1.53	1.54	1.55	1.55	1.56	1.61	1.45	1.58	1.64	1.56	1.63	1.62	1.65
Na ₂ O	6.24	6.16	6.48	6.23	6.35	6.30	6.17	6.49	5.88	6.24	6.56	6.27	6.35	6.47	6.24
K ₂ O	6.90	7.12	6.81	6.94	6.98	6.88	7.06	6.23	6.69	6.83	7.04	7.01	7.01	6.94	7.00
P ₂ O ₅	0.10	0.09	0.06	0.06	0.06	0.06	0.07	0.13	0.06	0.10	0.12	0.10	0.12	0.10	0.1
Total	100.00	100.00	100.00	100.00	100.00	100.00	100.00	100.00	100.00	100.00	100.00	100.00	100.00	100.00	100.00
V	39	36	37	36	40	40	39	42	42	40	40	29	40	39	39
Cr	1	2	2	2	3	2	2	1	3	3	0	2	0	0	2
Co	5	6	6	5	6	6	6	7	6	6	6	5	6	5	5
Ni	6	6	5	6	7	6	6	6	6	6	6	6	6	6	6
Rb	310	305	309	304	310	309	306	305	314	310	304	308	307	303	302
Sr	53	59	57	72	60	69	68	66	58	55	69	69	61	71	62
Y	29	29	29	29	29	29	29	29	29	29	29	29	29	29	29
Zr	487	475	470	480	485	465	470	471	502	489	470	475	477	463	471
Nb	69	68	67	66	70	67	66	68	72	70	68	69	69	66	69
Ba	204	216	206	229	201	221	229	221	202	215	207	219	223	227	235
La	79	75	71	72	75	75	77	73	68	76	74	73	77	69	76
Ce	152	142	154	166	158	115	150	135	150	145	143	143	130	125	139
Th	39	47	43	31	33	38	48	32	37	38	34	39	42	35	49
U	13	17	13	11	11	13	14	12	12	11	12	13	16	11	18

TABLE 3

Isotopic data

Sample	$^{87}\text{Sr}/^{86}\text{Sr}$ W-r	$^{87}\text{Sr}/^{86}\text{Sr}$ K-f
OIS 200 A	0.70610 ± 1	0.70606 ± 1
OIS 200 D ₁	0.70602 ± 1	0.70604 ± 1
OIS 200 G ₆	0.70605 ± 1	0.70608 ± 1

fectured by contamination. The differences in the Sr-isotope ratio of the whole-rock samples suggest that contamination occurred during or after eruption.

The results of the geochemical analyses indicate that a chemically and isotopically homogeneous batch of magma was drained during the eruption of the CT.

Pumices of the Cretaio Tephra

The formation and growth of vesicles to form pumice has been of interest to geologists for over 2000 years. Verhoogen (1951), in an elegant analysis of bubble nucleation, growth and rise in the magma, concluded that volcanic ash formed when expanding bubbles coalesced. That is most likely correct for lava fountains of low-viscosity magmas, but not for the pumice formation; pumice, "a highly vesicular pyroclast with low bulk density and thin vesicle walls" cannot exist if all bubbles coalesced and disintegrated. McBirney and Murase (1970) showed that the rate of bubble rise within a magma is far too slow to be responsible for pyroclast formation by bubble coalescence. Rittman (1936) and Bennett (1974) proposed disruption of a vesicular magma by shock decompression; this appears to be a realistic model, but Bennett's ideas fell short when he proposed that pumice and ash are formed by melt condensation. Condensation of a melt to a droplet hardly fits the description of a pumice clast.

Before analyzing bubble (vesicle) growth histories, investigators need data on the size

distributions and shapes of vesicles. This is an extremely difficult task, especially since the three-dimensional aspects of a pumice must be measured. Various approaches have been used, including: (1) modeling vesicle growth, based on physical and chemical properties of volatiles in a silicate melt (Sparks, 1978); (2) the tedious and difficult task of manually measuring vesicles using stereo scanning electron micrograph images (Heiken, 1987); (3) modal analysis of thin sections; and (4) a variety of impregnation techniques (Whitham and Sparks, 1986). All of these methods have produced interesting and useful results, but generally lack accuracy and, more importantly, the number of measurements required for statistical analysis. The Cretaio eruption sequence offers an excellent opportunity for the study of vesicle nucleation and growth.

Vesicularity. Vesicle volumes (vesicularities) within pumice clasts range from 63 to 77% (Fig. 4). There is no systematic change throughout the entire Cretaio pumice fall sequence or even within individual members.

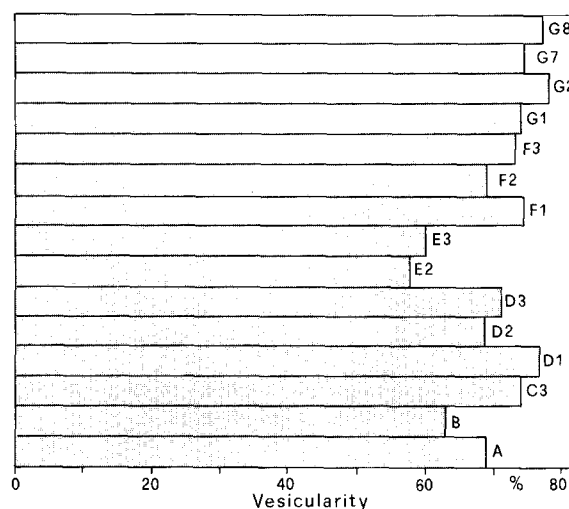


Fig. 4. Percent vesicles, measured on polished thin sections with SEM and image analysis program. There is no systematic variation throughout the eruption sequence. The degree of vesiculation is slightly less in hydrovolcanic units (B and E), where vesicle growth may have been suppressed by magma/water interaction in the conduit.

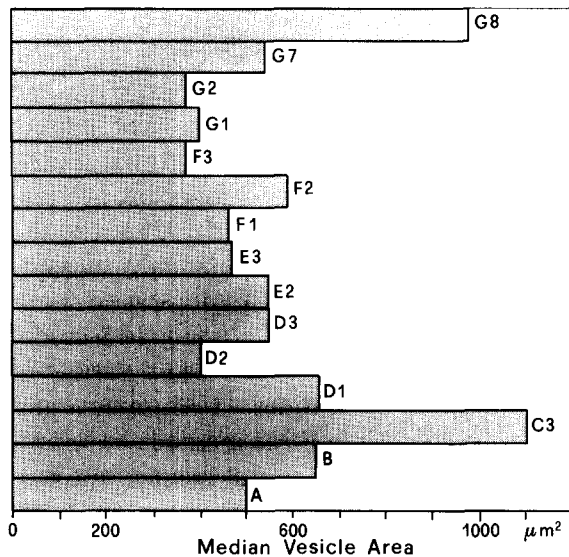


Fig. 5. Variation in median vesicle size (μm^2) or "area" throughout the eruption sequence. The only systematic variation is within pumice clasts from the lowest three members (A–C).

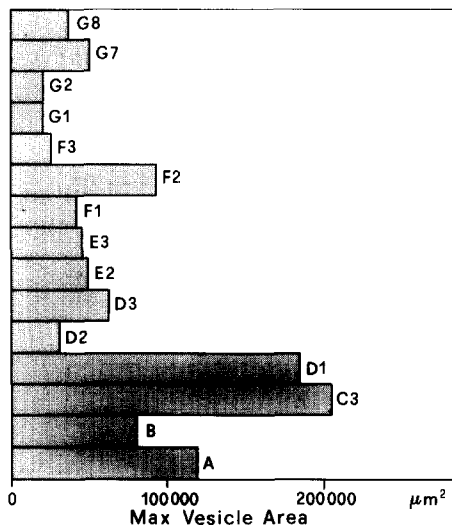


Fig. 6. Variation in maximum vesicle size (μm^2) within pumices sampled from the eruption sequence.

This uniformity follows the geochemical homogeneity of the magma chamber proposed on the basis of magma chemistry. Pumices from member E have lower vesicularities, perhaps related to suppression of vesiculation below the vent by magma/water interaction; E has been interpreted in the field and by size analysis to

have been of phreatomagmatic origin.

Vesicle size. Median vesicle size (area) ranges from 500 to 1100 μm^2 (equivalent radius = 12 to 18 μm). Within the lowest three units (A to C3) there is a systematic increase in median vesicle size (Figs. 5 and 6); above this, there is no systematic change in vesicle size. Throughout the complete eruption sequence, however, there appears to be an upward decrease in maximum vesicle size (Fig. 6).

Vesicle size distribution. All samples have a normal distribution of vesicles between 0 and 3000 μm^2 (equivalent radius = 0 to 30 μm) (Fig. 7). Deviation from the normal distribution at > 11,000 μm^2 (eq. radius = 59 μm) occurs when there is vesicle coalescence; without coalescence, distribution would be normal and not exhibit any bimodality. The effect of coalescence on size distributions can be seen in examination of the scanning electron micrographs (Fig. 8).

Shape factors. Shape factors are a measure of the vesicle complexity (cross-section of a sphere = 1). When plotted against area, it can be seen that shape factor increases with size as vesicles first coalesce (essentially a grouping of touching vesicles connected by small tubes), then decreases as the pockets of coalesced vesicles continue to expand and vesicle walls flatten and anneal (Fig. 9).

Within units A and B, F1 to F3, and G1 to G8, there is evidence for systematic coalescence of vesicles (increasing shape factor with increasing area). In units C3 to E3, there is a kink in the curve at 21,000 μm^2 (eq. radius = 82 μm) and shape factor of 23 to 40, showing the expansion of pockets of coalesced vesicles and flattening of septae remaining from individual broken vesicle walls. These decreasing shape factors require a lower overall viscosity; this lower viscosity is also evident in pumice from E2, which shows flattened vesicle walls.

Vesicles measured in pumices from this Plinian eruption sequence show no systematic

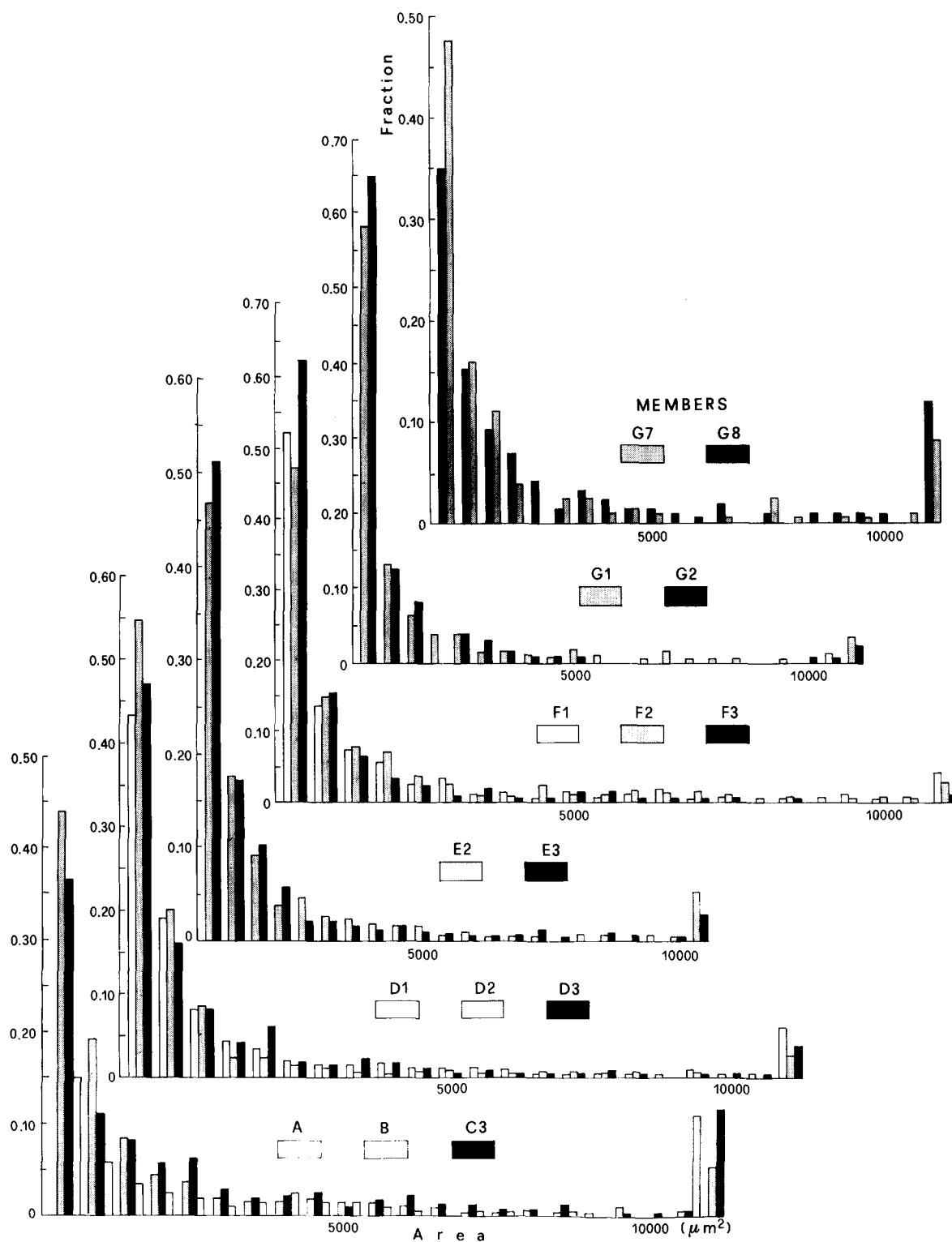


Fig. 7. Bargraphs showing distribution of vesicle size (areas) within pumices from each subunit of the Cretaio eruption sequence. Measurements were made to 120,000 μm^2 (equivalent radius = 195 μm). The x-axis is cut at 12,000 μm^2 to fit the diagrams on to a page. The vesicle sizes are normally distributed to 3000 μm^2 (eq. radius = 30 μm). Above 3000 μm^2 , vesicles are coalesced vesicles (connected vesicle cluster) with random sizes up to 120,000 μm^2 . The bars on the right consist of the sum of vesicle sizes between 12,000 and 120,000 μm^2 .



Fig. 8. Scanning electron micrograph of a polished, ion-etched thin section of a pumice clast from Cretaio subunit D. For each unit, vesicles were measured for area, perimeter, shape factor, diameter, length, width, aspect ratio, and orientation. The larger vesicles are coalesced vesicles, accounting for bimodality of vesicle sizes.

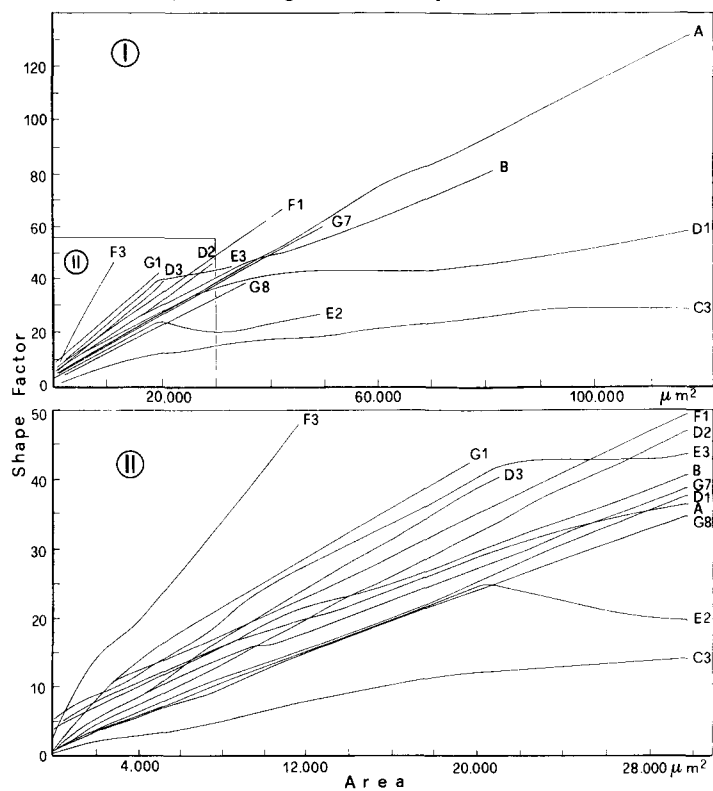


Fig. 9. Vesicle size (area) vs. shape factors for Cretaio pumices. Letters represent members within the eruption sequence. Increasing shape factors represent increasing vesicle complexity. Complexity of vesicle shapes increases with increasing coalescence of vesicles. (II) represents distribution of vesicle size (area) vs. shape factor between 0 and 30,000 μm^2 .

variation from the base to the top of the eruption sequence. The magma feeding this eruption appears to have had more or less the same volatile content, flux, and bubble growth behavior. Vesicle area distributions are normal, indicating one period of vesicle nucleation and growth. There is a bimodality of vesicle sizes and shapes within pumices from many units, but it is related not to growth, but to the degree of vesicle coalescence. Some of the pumices erupted were hotter and less viscous than others (middle of the eruption sequence), as reflected by decreasing shape factors for pockets of coalesced vesicles and partly collapsed vesicles. For the Cretaio pumices, the single generation of vesicle growth as proposed by Sparks and Brazier (1982) applies. Although all eruptions are different, perhaps some earlier work where two generations of vesicle growth are proposed (e.g., Heiken, 1978) should be re-examined with these observations in mind.

Areal and sequential variation of grain size

Whole sample character

The following descriptions present both the log-normal and sequential fragmentation/transport (SFT) character of the Cretaio samples. As described earlier, six members are designated in ascending stratigraphic position by letters A through G, respectively. Members A, C, D, F, and G are pumice fall deposits that show a clast-supported fabric. Member B shows a matrix-supported fabric and is characterized as an ash and pumice fall deposit. Its poor sorting suggests some reworking, hydrovolcanic fragmentation and/or surge transport. Member E is best characterized as a surge deposit (Fig. 10).

Overall, 6 subpopulations are present in most samples; subpopulation 1 is the coarsest and subpopulation 6 the finest. Table 4 lists the

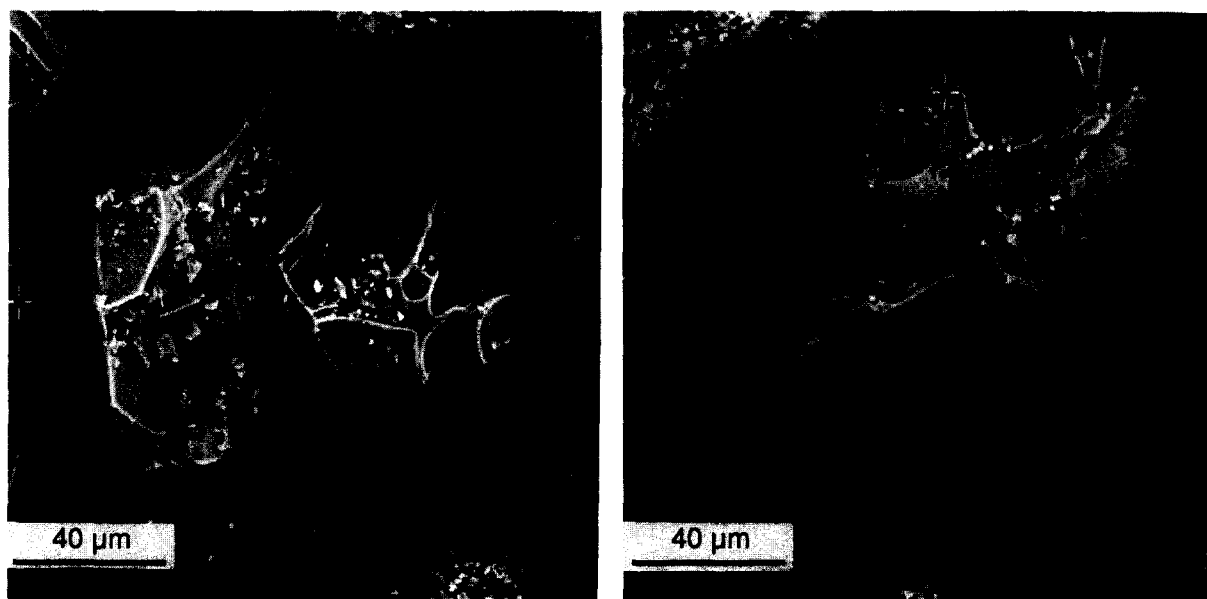


Fig. 10. Scanning electron micrograph of ash from member E. The fine-grained ash from this matrix-supported member consists of simple shards of $< 40 \mu\text{m}$ and complex shards from the common walls of closely spaced vesicles.

TABLE 4

Cretaio subpopulations

Subpopulation	Mode (ϕ)	Dispersion (γ)	Fraction
1*	-3.79	-0.64	0.14
2	-2.40	-0.65	0.26
3	-1.21	-0.82	0.34
4	0.10	-0.53	0.12
5	2.74	-0.74	0.06
6*	4.26	-0.59	0.07
Whole	-0.35	-0.66	1.00

*Subpopulation whose character is partly affected by data truncation.

characteristics of these subpopulations. Because sieving results in addition of particles whose diameter is greater than -5ϕ to the -4.0ϕ fraction and no data for particles finer than 4ϕ , some of the modes for subpopulations 1 and 6 are artificial, and these subpopulations are not considered reliable for interpretation. For example, the dispersion values for these subpopulations are greater (better

sorted) than they would be if data were not truncated.

The results of grain-size analyses can be presented in histograms shown as cubic spline curves that pass through each data point (Fig. 11). Original sieve fractions can be extracted from the plots at points halfway between each full ϕ interval. Figure 11 (I) presents average distributions for pumice fall samples for members A, C, D, F, and G. To obtain these average data, SFT fit parameters were averaged for each member. Beside the evident polymodal character, these curves show that earlier eruptions (members A and C) produced somewhat finer peaks than did later eruptions (members D, F, and G). Figure 11 (II) shows a similar histogram, which characterizes an average for all these pumice fall samples and the subpopulations present, which contribute to the average distribution. (III) and (IV) in Figure 11 are histograms for the ash and pumice fall (member B) and surge deposit (member E),

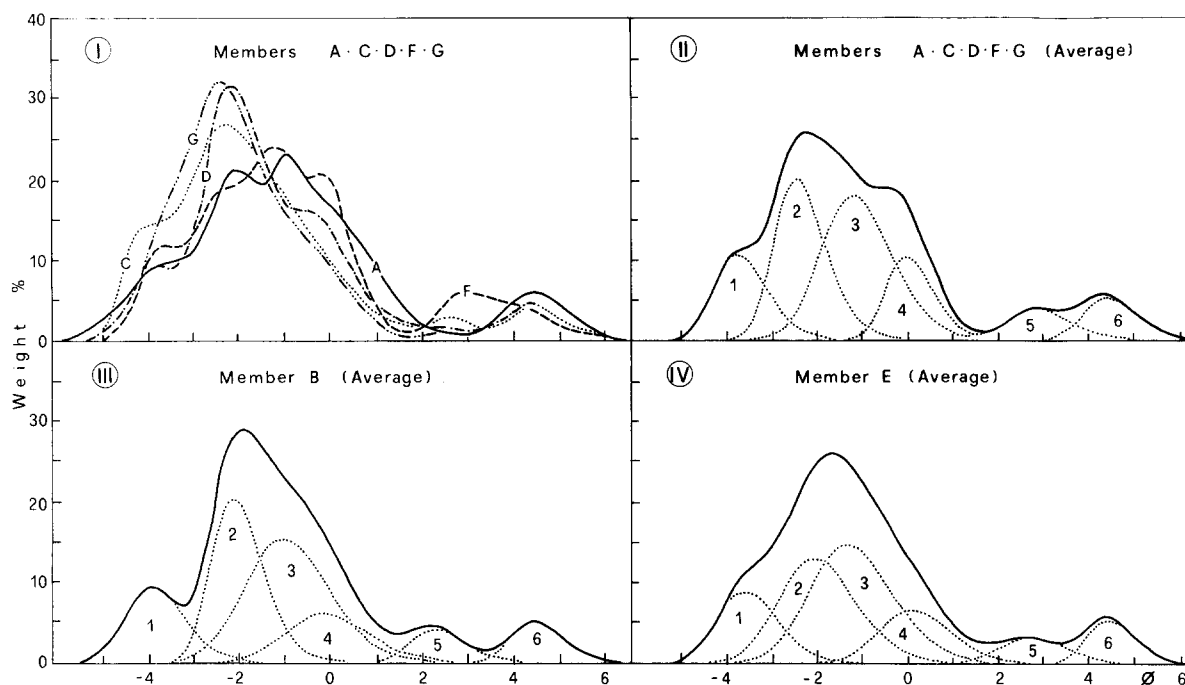


Fig. 11. Histograms of average tephra size distributions calculated from subpopulation parameters of the samples. (I) Average pumice falls from member A, C, D, F, and G. (II) Average of all subpopulations 1 through 6. (III) Average of ash and pumice fall member B and its constituent subpopulations. (IV) Average of surge member E and its constituent subpopulations.

TABLE 5

Cretaio subpopulations by deposit type

Subpopulation	Mode (ϕ)	Dispersion (γ)	Fraction
Pumice falls			
1*	-3.79	-0.63	0.15
2	-2.45	-0.63	0.28
3	-1.20	-0.81	0.35
4	0.04	-0.54	0.13
5	2.84	-0.72	0.06
6*	4.35	-0.61	0.07
whole	-0.56	-0.65	1.00
Ash and pumice fall			
1*	-3.98	-0.71	0.15
2	-2.15	-0.61	0.28
3	-1.07	-0.86	0.35
4	-0.19	-0.85	0.13
5	2.25	-0.65	0.06
6*	4.39	-0.59	0.07
whole	0.02	-0.71	1.00
Surge			
1*	-3.65	-0.73	0.15
2	-2.09	-0.84	0.28
3	-1.36	-0.86	0.34
4	0.06	-0.81	0.13
5	2.69	-0.79	0.06
6*	4.37	-0.53	0.07
whole	-0.56	-0.74	1.00

*Subpopulation whose character is partly affected by data truncation.

showing their respective subpopulation character. Table 5 lists subpopulation parameters for three deposit types. It is interesting to note that these three deposit types all show very similar subpopulation characteristics, especially for the fractions present for each subpopulation, which are nearly identical among the deposit types. The main differences exist in the dispersion values and slight variation in the mode size for each subpopulation.

Whole population standard deviations have been plotted, in Walker (1971) type diagrams, versus mean diameter for the pumice falls, ash and pumice fall, and surge deposit (Fig. 12). These plots show that the pumice fall samples generally plot within the fallout field (Fig. 12 (I)). Surge samples clearly plot within the

massive and planar surge field for silicic tephra (Sheridan and Wohletz, 1983), but not in the sandwave field (Fig. 12 (II)); no distinct dune bedforms were seen in the field. While the matrix-supported ash and pumice fall deposit also plots in the surge field, two points lie outside, suggesting that perhaps some of member B is fallout and some is surge deposit.

There is an overall decrease of mean diameter with distance (member A excluded because there is only one sample) (Fig. 13). The mean diameter decrease with distance is larger for later eruptive units. Ash and pumice fall member B shows a more enhanced decrease with distance than does the surge member E (Fig. 13 (II)).

Subpopulation analysis

For all samples, subpopulations 2 and 3 are the dominant constituents (Table 4). A best fit polynomial curve on a plot of subpopulation weight fraction versus their modes (Fig. 14) generally reproduces an average spline fit for the Cretaio samples, with a peak near -2ϕ and another in the fine fractions near 4ϕ . In a comparison of the three main deposit types, the frequency of subpopulations as a function of a mode size nicely illustrates how the general distribution of subpopulation modes is coarser for pumice falls than for ash and pumice fall and surge members, the latter two showing significant modes near 4ϕ (Fig. 15).

Overall, subpopulation dispersion fractions are greatest for gamma (γ) values near -0.95 and fall off exponentially as γ increases. Truncated subpopulations 1 and 6 show relatively high fractions for a given dispersion (γ) value, signifying their peaked nature caused by the data truncation (Fig. 16). Subpopulations 2 and 3 appear to have higher fractions for a given γ value than do subpopulations 4 and 5, which indicates their better development, or distinct occurrence. The surge deposit shows the widest range of significant γ values, fol-

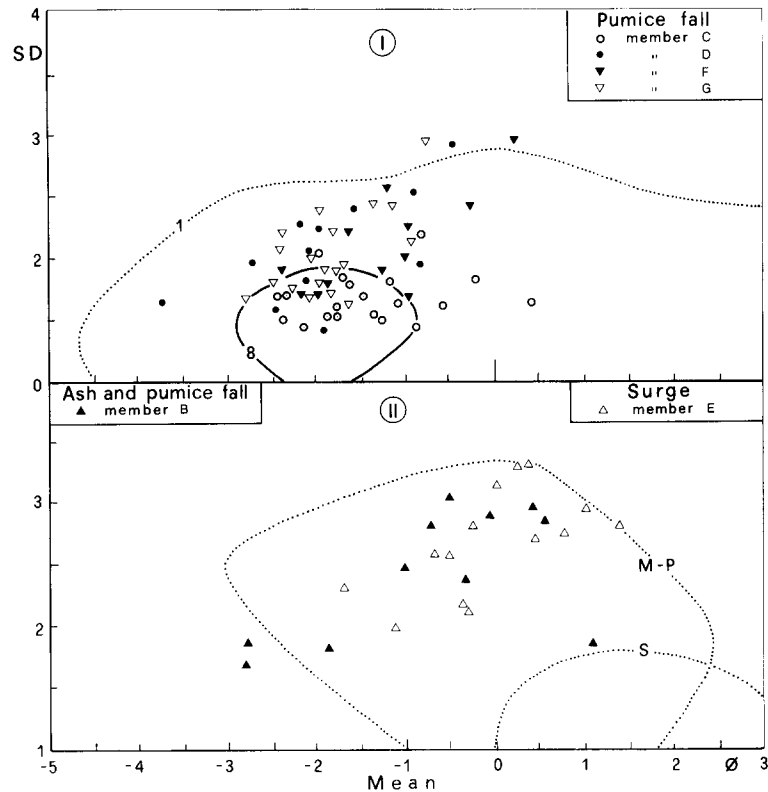


Fig. 12. (I) Walker (1971) type standard deviation versus mean diameter plot of pumice fall samples, showing 1 and 8% contour lines for fall out samples of Walker (1971). (II) Standard deviation versus mean diameter for ash and pumice member *B* and surge member *E*. Dashed lines enclose the field of silicic surge deposits of Sheridan and Wohletz (1983) where *M-P* designates the massive and planar surge field and *S* the sandwave surge field.

lowed by that of the ash and pumice layer, with the lowest range of γ values noted for the pumice falls, which are generally less than -0.6 (Fig. 17). Gamma values generally increase with decreasing mode sizes, such that subpopulations 2 and 3 show dispersion (γ) values near -0.9 , while subpopulations 5 and 6 range around -0.6 (Fig. 18). The best fit curve rises to high values of dispersion for subpopulations coarser than -3.0 , which is somewhat artificial because of truncation, as is that of the curve through subpopulation 6.

This range of γ values for these deposit types is predicted by Wohletz et al. (1989), who showed that ballistically emplaced deposits typically develop size distributions with γ values from -0.9 to -0.6 , because of the mass/size dependency of ballistic transport. Suspen-

sion transport of tephra, where aerodynamic drag greatly affects the mass/size dependency of transport, results in higher γ values, ranging from -0.7 to near 0.0 , but near -0.3 for well developed suspension transport. Saltation and traction mode transport in pyroclastic surges and flows or during reworking of fallout deposits have expected mass/size dependencies represented by γ near -0.6 ; traction deposits evolve little from this γ value, but well developed saltation may cause increase of γ to greater than 0.0 . Gamma values of greater than 0.0 are indicative of particle aggregation where finer particles stick together, and the fine skewness of the distribution decreases. Also, if the initial tephra fragmentation has a hydro-volcanic component, γ values will be higher than if the fragmentation were solely mag-

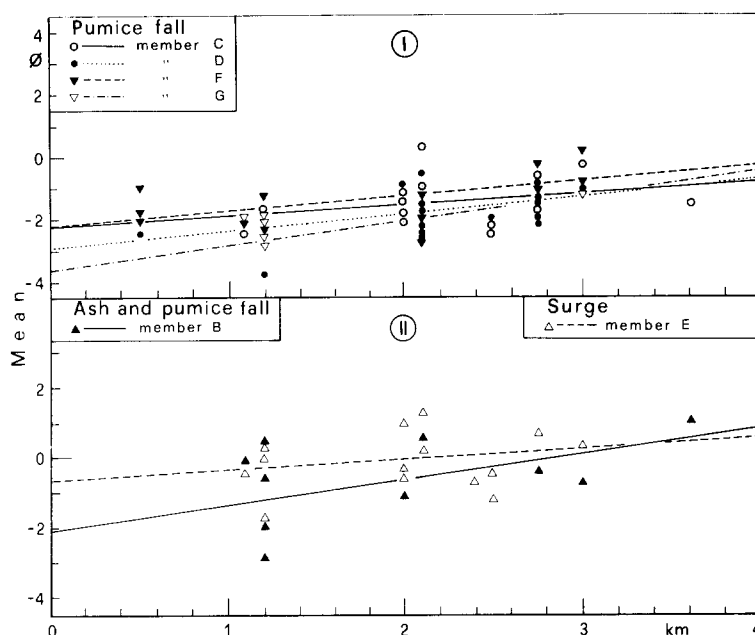


Fig. 13. Mean diameter versus distance from the vent for pumice falls (I) and ash and pumice layer with surge layer samples (II). Lines represent best fits to each layer.

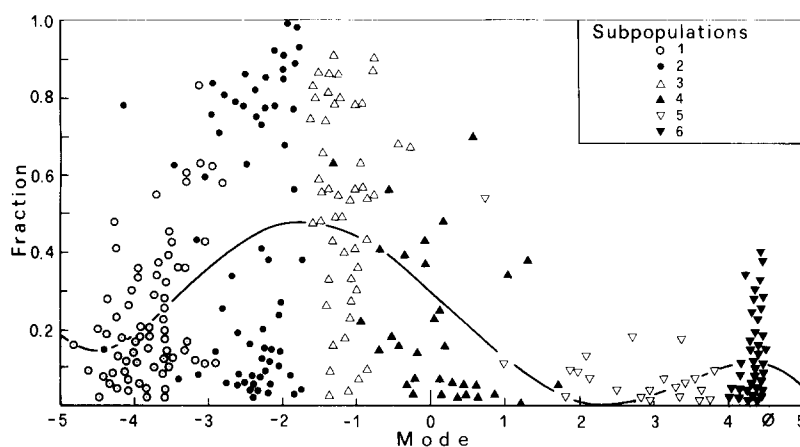


Fig. 14. Subpopulation fraction versus mode size for each subpopulation sample; subpopulations are designated by numbers 1 to 6.

matic. For magmatic eruptions, the initial distribution of planes of weakness determine the range of tephra sizes produced, so that vesicle and crystal sizes greatly determine the γ value resulting from this type of eruption.

From these considerations, we can interpret

the following subpopulations with some confidence.

(1) Subpopulation 2 represents ballistically transported particles.

(2) Subpopulation 3 includes those that likely have been part of the traction carpet in a surge

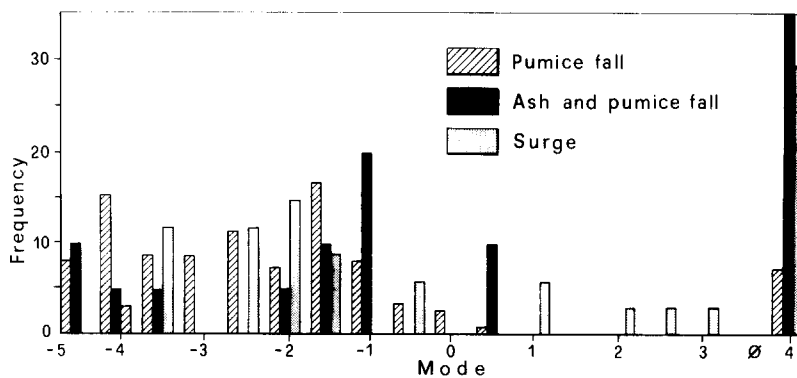


Fig. 15. Histogram of subpopulation mode frequency for pumice fall, ash and pumice fall, and surge units.

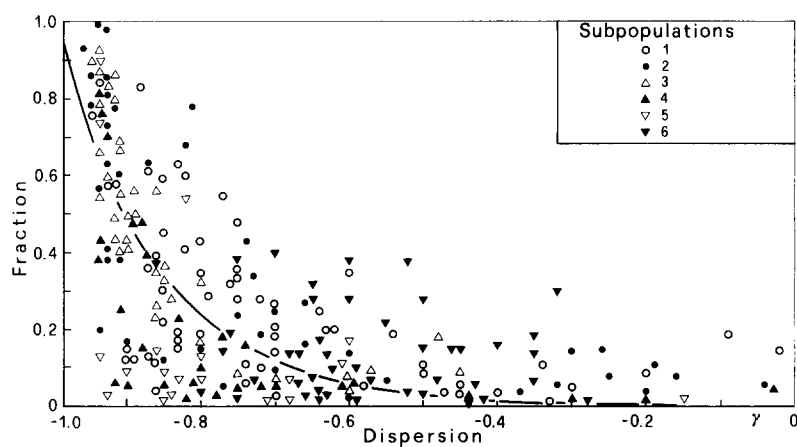


Fig. 16. Subpopulation fraction versus dispersion value (γ). Each subpopulation value is plotted by number.

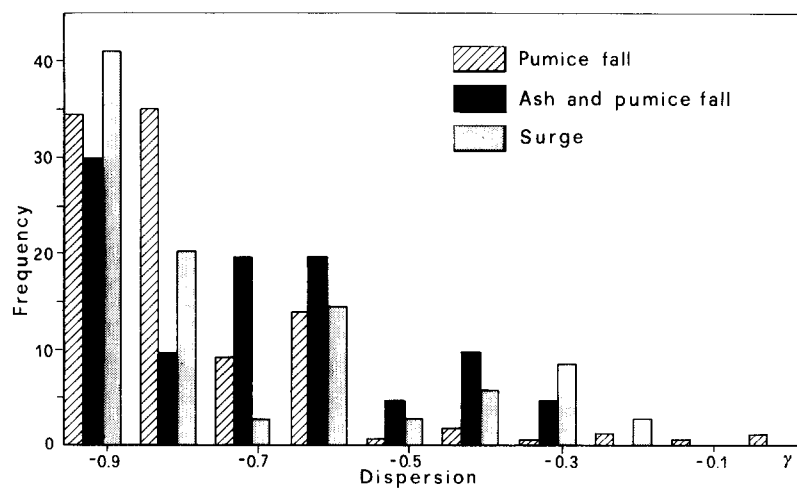


Fig. 17. Histogram of subpopulation dispersions (for those subpopulations with fractions greater than 0.10).

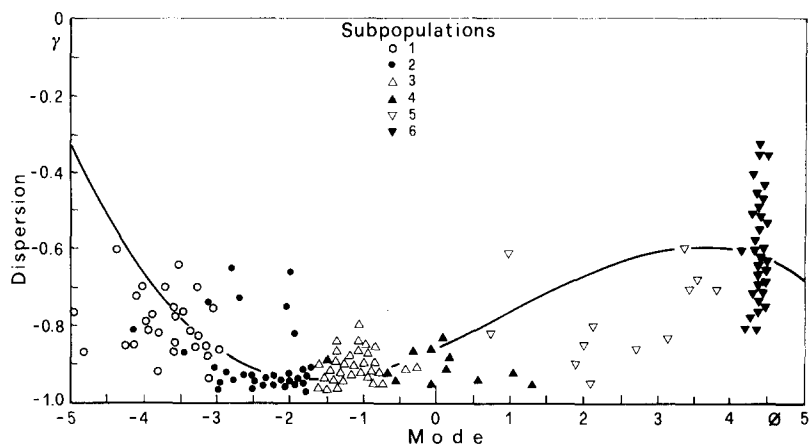


Fig. 18. Dispersion plotted as a function of subpopulation mode size.

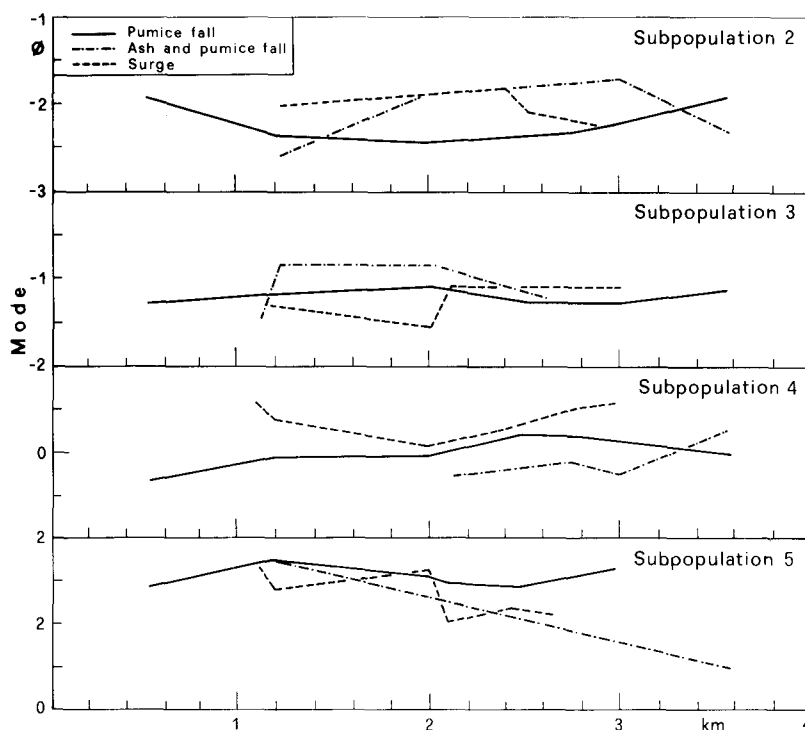


Fig. 19. Subpopulation mode size versus distance from the vent for subpopulations in each of the three main deposit types.

or reworked from earlier deposited tephra.

(3) Subpopulation 4 represents tephra whose size range can readily be carried by saltation.

(4) Finally, subpopulation 5 represents particles that are greatly affected by aerodynamic drag and turbulence such that they have likely been suspended during transport.

Transport distance evolution

The subpopulation mode size varies with distance as a function of the three main deposit types (Fig. 19). The ballistic mode subpopulation 2 shows a general fining with transport distance and the traction mode

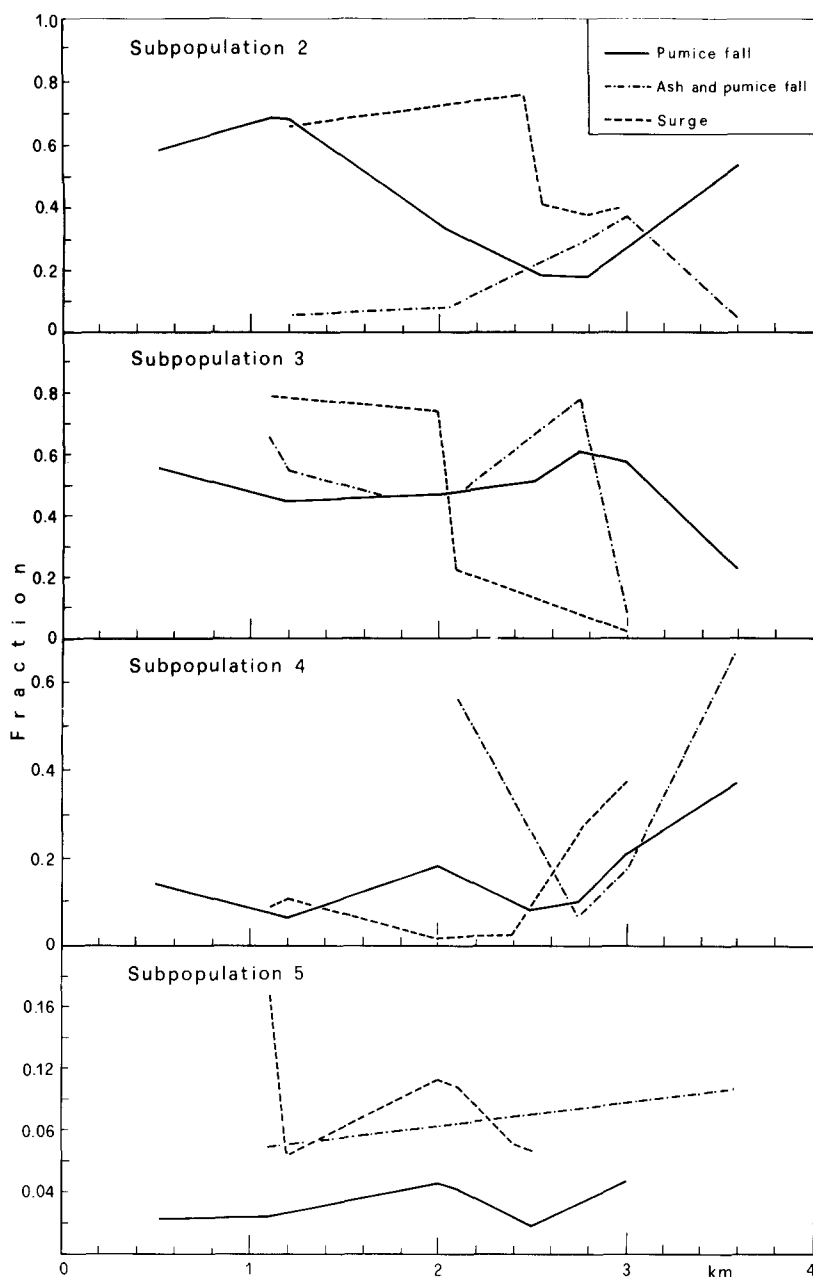


Fig. 20. Subpopulation fractions versus distance from the vent for subpopulations in each of the three main deposit types.

subpopulation 3 stays fairly constant in size with distance. Note the inflections of these smoothed curves between distances of 2.0 to 2.4 km from the vent, which will be shown to have some significance in a subsequent plot (Fig. 20). Saltation reworking of pumice falls

generally affects finer tephra with distance (subpopulation 4). Surge tephra first coarsen in this mode (subpopulation 4) and then fine. The suspended pumice fall subpopulation 5 shows a general coarsening with distance, which might suggest some fine particle aggre-

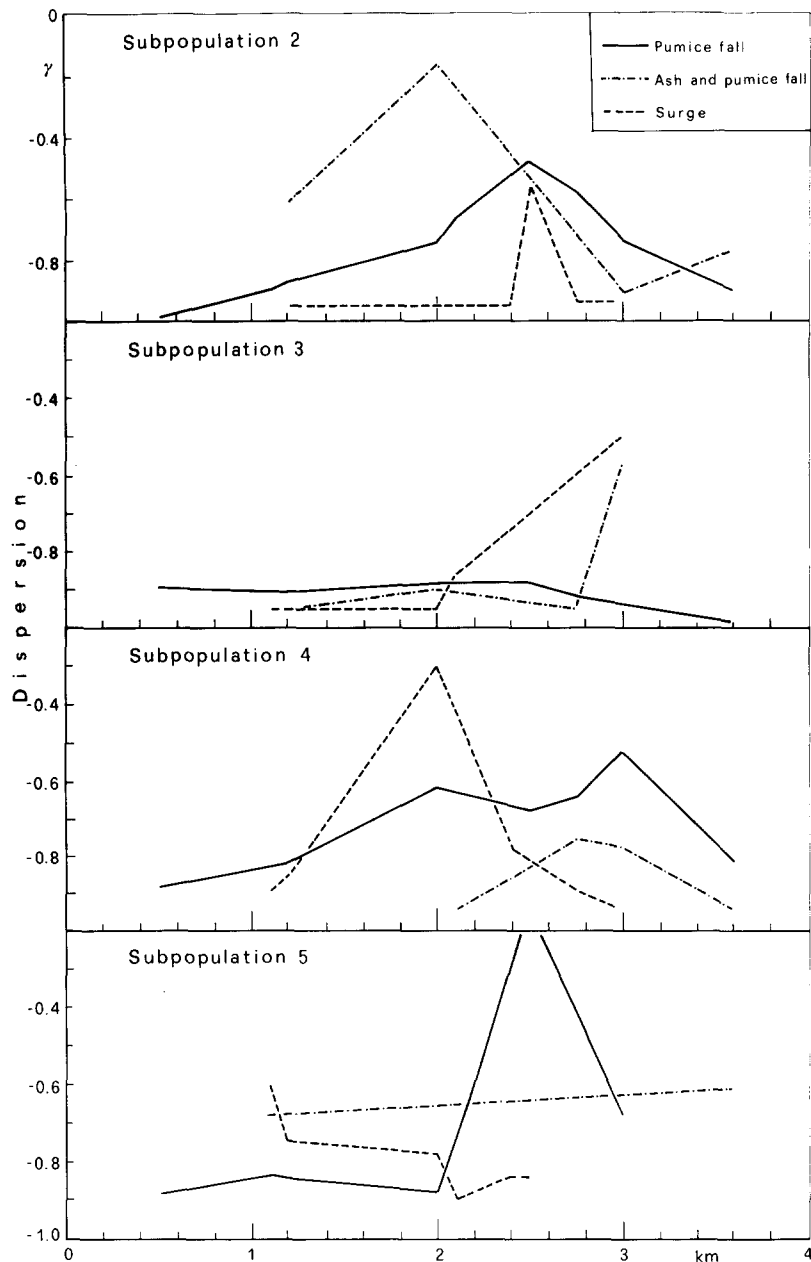


Fig. 21. Subpopulation dispersion values versus distance from the vent for subpopulations in each of the three main deposit types.

gation, an observation supported by the distance evolution of its γ values.

Variation of the subpopulation fractions with distance from the supposed vent area are shown in Figure 20. Subpopulation 2 in the pumice fall deposits generally decreases with

distances out to a distance of 2.6 km and then begins to rise, whereas it is increasing out to 3.0 km in the ash and pumice fall layer, after which it falls. In the surge deposit, this ballistic mode gradually increases in abundance out to 2.4 km where it falls sharply. The traction mode

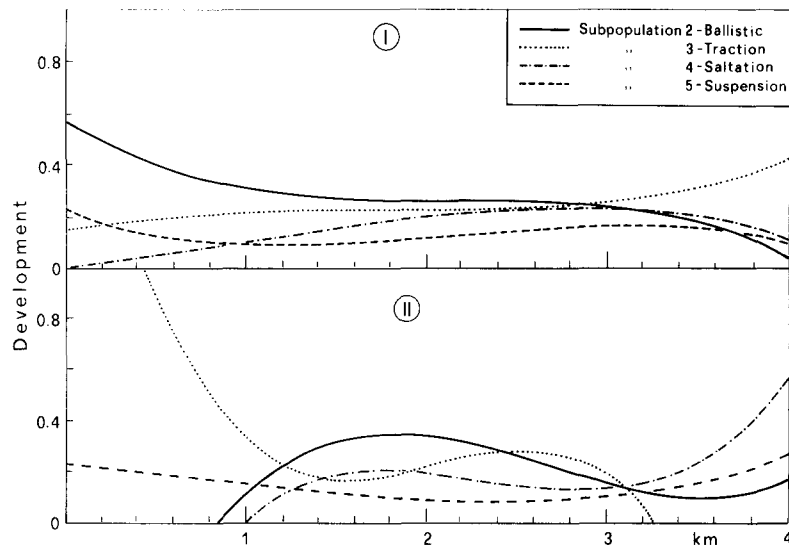


Fig. 22. Plots of subpopulation development factor versus distance where each subpopulation is shown to be likely transported by the mechanism shown. (I) Fallout tephra are dominantly transported by ballistic and suspension mechanisms. Traction mechanisms. (II) Surge tephra are dominantly transported by laminar flow in a traction carpet and saltation. Subordinate transport by ballistic trajectory and suspension are also somewhat developed.

subpopulation 3 also shows a rapid decline in surge layers at about 2.0 km, whereas at that distance the ash and pumice fall layer shows a rapid increase. For the pumice fall, traction reworking gradually increases out to about 2.8 km after which it falls off. For saltation transport mode 4 there is a gradual increase in saltation reworking of pumice fall layers out to 2.0 km after which it decreases in importance but later rises again after 2.4 km. For the ash and pumice deposit, saltation also declines over the interval between 2.0 and 2.8 km. This decline in the degree of saltation deposition is rapid but is followed by a rapid increase beyond 2.8 km. For surge deposits there is a general decline in saltation mode transport out to 2.4 km after which it rapidly rises. Suspension transport of subpopulation 5 generally increases with distance for the pumice fall deposits and ash and pumice deposit, but shows two sharp inflections at 1.2 and 2.0 km in the surge deposit.

In evaluating the development of the individual transport modes, dispersion (γ) increases generally indicate an increasing dis-

tinction of the transport mode (Fig. 21). The ballistic mode evolves with distance out to a range of 2.5 km in the pumice falls and surge deposit and 2.0 km for the ash and pumice deposit, after which it then becomes less distinct. Although the traction mode reworking of pumice falls remains poorly developed for all distances, it becomes very pronounced at distances greater than 2.0 km in the ash and pumice fall deposit. Traction flow in the surge becomes increasingly developed after 2.0 km of transport. Saltation reworking of pumice falls and the ash and pumice deposit generally becomes more developed out to distances of about 2.8 to 3.0 km, after which its development declines. For the surge deposit, saltation is best developed at a distance of about 1.9 km, after which it falls off. Suspended transport development shows a peak at a distance of 2.5 km in the pumice falls, suggesting a range where aggregated particles experience premature fallout. Suspension gradually increases with distance for the ash and pumice fall, but shows a stepped decline with distance for the surge deposit.

Fallout facies

The variation in subpopulation fractions and γ developments (Figs. 20 and 21) were combined into a single development parameter, a simple additive function of the abundance (fraction) and evolution (γ). For fallout deposits, ballistic transport decreases in development (importance) with distance, and suspension becomes more developed and important (Fig. 22 (I)). Concurrently the importance of traction and saltation reworking generally increases with the transport distance. From this analysis, fallout facies are expected to show more and more ash component with distance and the increased likelihood for a layered fabric to show up.

Surge facies

Within surge deposits, traction transport dominates emplacement near the vent, with saltation becoming slightly dominant from about 1.4 to 2.0 km, after which traction flow again is dominant (Fig. 22 (II)). At distances beyond 3.2 km, saltation is again the best developed transport mode. Suspension does not vary much with distance, such that a fine ash component is generally present, and the ballistic component becomes somewhat important beyond 1.2 km. Because saltation never reaches a very high degree of development, dune deposits are not expected to be present, as has been observed in the field. A surge facies model for this deposit, based upon relationships described by Wohletz and Sheridan (1979) is as follows: (1) from the vent outward to about 1.2 km, traction transport is well developed, and the surge bedding should have a laminar (planar) character but with a fine ash component making bedding less distinct; (2) for distances from about 1.4 to 3.2 km, where both traction and saltation show similar levels of development, massive surge beds are expected; (3) beyond 3.2 km, where the surge has pinched out, most of surge is expected to have

been reworked by traction flowage during rain water runoff and by saltation during windy periods. We point out that this facies distribution does not fit the proximal to distal model of Wohletz and Sheridan (1979). This result is likely a function of the paleotopography, with slopes increasing with distance from the vent, which could have promoted reinflation of the surges by increased turbulence and incorporation of air. A break in the paleoslope between 2 and 3 km from the vent, where the slope is nearly level, apparently caused the distinct fluctuation in subpopulation parameters seen in Figures 20 and 21.

Conclusions

The Cretaio Tephra is the product of one of the many historical eruptions of trachytic magmas on the island of Ischia. Most of these youthful eruptions are from tuff ring-dome complexes located along faults crossing the eastern half of the island. The vents, including that for the CT eruption, are located along a line of N-S trending faults that bound the east side of the Mt. Epomeo resurgent block.

The Cretaio ^{14}C age of 1971 a B.P. agrees with the archaeological evidence of pottery found in underlying and overlying paleosols. The volume of erupted magma, although difficult to measure, as only part of the deposit fell on the island, was $<0.02 \text{ km}^3$ DRE. Seven subunits comprise the Cretaio Tephra; five are pumice and ash fallout deposits and two are hydrovolcanic surges.

The vent for the CT is not visible in the field, but buried by tephra deposits from later eruptions at Montagnone and Bosco della Maddalena. The vent location was inferred, based on the variations in subunit thicknesses.

The chemical and isotopic composition of the erupted magma did not change significantly during the eruption which perhaps was associated with dome growth.

For the Cretaio Tephra eruption there was not any concentration of volatiles near the top

of a magma reservoir, but a steady release of volatiles throughout all phases of this explosive eruption. Heiken (1987) showed an overall decrease in vesicularity through the eruption sequence of the Minoan Tuff, which is observed also in many other large-volume eruptions, where decreasing volatile content from a shallow, zoned magma chamber is proposed (e.g., Smith, 1979). Uniformity of vesicle volumes, sizes, and shapes and of chemical and isotopic composition throughout the eruption sequence indicates that there was little variation within the erupted magma. The small volumes of erupted magma and the alignment of vents suggest that eruptions were fed from the tops of N-S-trending, dike-like, rapidly emplaced bodies where differentiation did not occur. Similar conclusions were reached for eruptions of rhyolitic magma from the Inyo craters and domes in eastern California (Eichelberger et al., 1988).

Facies distributions within the CT are based on detected variations in sequential fragmentation/transport theory (SFT) characteristics of the fallout and surge members. The significant changes in subpopulation characteristics of CT surge deposits at distances of between 2 and 3 km may be related to the levelling of the slope. Subpopulations in the fallout tephra are affected by vesicle size populations above and below an equivalent diameter of about 3.5ϕ , which affects the abundance of subpopulations 4, 5 and 6.

The results of SFT analysis, together with stratigraphical and textural evidences, have allowed us to reconstruct a detailed picture of the emplacement of each tephra unit. After initial hydromagmatic eruption of member A, member B was deposited as an ash and pumice bed that shows characteristics of both fallout and surge emplacement. The higher γ values and the finer, less sorted nature of this member suggest a hydrovolcanic component. This conclusion is supported also by the slightly lower vesicularity of the pumice of this member (possible suppression of vesiculation by magma/water

interaction in the vent). The remaining eruptive episodes were dominantly sub-Plinian, except for member E, which is a fine-grained surge deposit; the high percentage of fine-grained particles in member E is indicative of a high degree of fragmentation, which likely occurred during water-melt interactions.

The variety of techniques used for this study can be used effectively together to make an interpretation of the nature of the shallow magma body, the homogeneous nature of the magma, and information on vesiculation, eruption, and distribution of the deposit; data necessary for creating volcanic hazard maps for the heavily populated island of Ischia.

Acknowledgements

The research has been supported by the Italian Gruppo Nazionale per la Vulcanologia—CNR. Work by Heiken, Wohletz, and Yu was done with partial support from Institutional Supporting Research at the Los Alamos National Laboratory and under the auspices of the U.S. Department of Energy.

Appendix—analytical methods

¹⁴C. For the chemical pretreatment of the samples, a “strong” acid-base-acid treatment (0.5 M HCl at 80°C for one hour, 0.1 M NaOH at 60°C for half an hour and 0.5 M HCl at 80°C for one hour) was used. The material was rinsed to pH 7 with distilled water between the steps. Following the chemical treatment, the samples were dried overnight in a 60°C oven. The samples were combusted in evacuated sealed quartz tubes, with copper oxide and silver wire for two hours at 950°C. In the presence of hydrogen, the carbon dioxide was reduced to filamentous graphite over a cobalt catalyst using the method of Vogel (Vogel et al., 1984, 1987). The resulting graphite-cobalt mixture was pressed onto copper targets for the measurement.

The ¹⁴C/¹²C and ¹³C/¹²C ratios were determined quasi-simultaneously and relative to the respective NBS oxalic acid I and PDB standard values (Bonani et al., 1987). The conventional radiocarbon ages were calculated using the procedure suggested by Stuiver and Polach (1977). They were corrected for natural fractionation and reported in years B.P. (before 1950). The results are listed

in Table 1. The errors quoted are at the 1σ level (one standard deviation).

The calibrated 2σ ^{14}C -age ranges (95% confidence limit; Table 1) were determined from the high-precision curve of Stuiver and Pearson (1986) based on dendrochronological dating. For this transformation the CalibETH program was used (Niklaus et al., 1991). It calculates the probability distribution, as described by Stuiver and Reimer (1986).

Sr isotopes. Sr was separated by a conventional ion-exchange technique and isotopically analyzed on single W filaments. Repeated analyses of NBS 987 standard yielded an average $^{87}\text{Sr}/^{86}\text{Sr}$ ratio of 0.710264 ± 5 (2σ). Typical total blank was less than 4 ng.

Image analysis of vesicles. For this study, we had to use two-dimensional slices through pumices for the purpose of measuring the distribution of vesicle areas. This is not as satisfying as a measurement of three dimensions, but with enough measurements, it provides a statistical view of vesicle distributions and shapes. Scanning electron micrographs of polished, ion-etched pumice samples were digitized and a binary image created of the vesicles. The binary image was analyzed using a Tracor Northern image analysis program (VISTATM). About 500 vesicles were measured for area, perimeter, shape factor [$\text{perimeter}^2 / (4\pi \text{ area})$], diameter, length, width, aspect ratio (length/width), and orientation. Vesicularities determined using this method are very accurate. We used the technique of size analysis using 2-dimensional thin sections of sandstones, developed by Friedman (1958), applied to the vesicle size distributions, but concluded that no adjustment was needed for this study.

Grain size. Ninety tephra samples taken at varying distances from the proposed vent area were dry sieved to characterize the size distributions of stratigraphic members A through G. Data were recorded at full-phi intervals from -4 (16.0 mm) to 4 (0.063 mm). Histograms of the data were converted to cubic spline curves passing through each data point such that original data are fully represented and can be easily extracted from the spline-curve plots. The spline curves were then analyzed by a computer program called SIZPOP. The program derives from SEQUEN, described by Wohletz et al. (1989), and allows separation and characterization of size distribution subpopulations, using either log-normal, sequential fragmentation, or sequential transport distributions. The resulting data fits explain more than 95% of the observed variance. In order to study the effects of the eruptive fragmentation and the subsequent transport upon the tephra size distributions, the sequential transport distribution was applied. Based upon the sequential fragmentation/transport theory (SFT) of Wohletz et al. (1989), this distribution is not empirical but is derived from the basic fragmentation physics and transport phenomena.

The main assumption of SFT is that resulting size distributions are functions of initial mass, and this mass is

subjected to sequential steps of fragmentation during eruption and later transport sorting events, also primarily functions of the mass of the individual particles being transported. This assumption is well supported by basic conservation laws of physics. SFT predicts that tephra size distributions will resemble log-normal distributions with skewing towards fine sizes, similar to that of Rosin and Weibull distributions. Because of varying particle density and shape, Wohletz et al. (1989) demonstrate that in conversion of mass distributions to diameter distributions, several subpopulations of size are to be expected. Furthermore, the functional dependence of mass upon fragmentation and transport mechanisms can be expressed by an exponent, γ , that determines the peak mode, standard deviation, and skewness of resulting distributions. γ is near -1 for broad, poorly defined distribution curves, which result from poorly evolved fragmentation and transport mechanisms that act upon the initial mass suddenly. As γ increases towards 0, distribution curves become more peaked, signifying better sorting. Wohletz et al. (1989) describe γ values for magmatic and hydro-volcanic fragmentation mechanisms as well as transport by ballistic trajectories, inertial flow in a traction carpet, particle saltation, and suspension. Because several of these transport mechanisms can sort the starting size population of tephra erupted, several subpopulation curves are expected to be generated within a given deposit.

References

- Bennett, F.D., 1974. On volcanic ash formation. *Am. J. Sci.*, 274: 648–661.
- Bonani, G., Beer, J., Hofmann, H.A., Wolfli, W., Pfeleiderer, C., Kromer, B., Junghaus, C. and Munnich, K.O., 1987. Fractionation, precision, and accuracy in ^{14}C and ^{13}C measurements. *Nucl. Instrum. Methods Phys. Res.*, B29: 87–90.
- Chiesa, S., Civetta, L., De Lucia, M., Orsi, G. and Poli, S., 1987. Volcanological evolution of the island of Ischia. In: P. Di Girolamo (Editor), *The Volcanoclastic Rocks of Campania (Southern Italy)*. *Rend. Accad. Sci. Fis. Mat. Naples, Spec. Iss.*, pp. 69–83.
- Civetta, L., Gallo, G. and Orsi, G., 1991. Sr- and Nd-isotope and trace element constraints on the chemical evolution of the magmatic system of Ischia (Italy) in the last 55 ka. *J. Volcanol. Geotherm. Res.*, 46: 213–230.
- Eichelberger, J., Vogel, T., Younker, L., Miller, C., Heiken, G. and Wohletz, K.H., 1988. Structure and stratigraphy beneath a young phreatic vent: South Inyo Crater, Long Valley, California. *J. Geophys. Res.*, 93: 13,208–13,220.
- Friedman, G.M., 1958. Determination of stave-size distribution from thin-section data for sedimentary petrological studies. *J. Geol.*, 66: 344–416.

- Heiken, G., 1978. Plinian-type eruption in the Medicine Lake Highland, California and the nature of the underlying magma. *J. Volcanol. Geotherm. Res.*, 4: 375–402.
- Heiken, G., 1987. Textural analysis of tephra from a rhyodacite eruption sequence, Thira (Santorini), Greece. In: J. Marshall (Editor), *Clastic Particles*. Van Nostrand-Reinhold, New York, pp. 67–78.
- McBirney, A. and Murase, T., 1970. Factors governing the formation of pyroclastic rocks. *Bull. Volcanol.*, 34: 372–384.
- Niklaus, T., Bonani, G., Simonius, M., Suter, M. and Wolfli, W., 1992. CalibETH—an interactive computer program for the calibration of radiocarbon dates. *Radiocarbon*, 34(3).
- Orsi, G. and Gallo, G., 1992. Volcanism at Ischia in the last 10 ka (in prep.).
- Orsi, G., Gallo, G. and Zanchi, A., 1991. Simple shearing block-resurgence in caldera depressions. A model from Pantelleria and Ischia. *J. Volcanol. Geotherm. Res.*, 47:1–11.
- Rittmann, A., 1936. *Vulkane und ihre Tätigkeit*. Ferdinand Enke Verlag, Stuttgart, 188 pp.
- Rittmann, A. and Gottini, V., 1980. L'isola d'Ischia-Geologia. *Boll. Serv. Geol. Ital.*, 101: 131.
- Sheridan, M.F. and Wohletz, K.H., 1983. Hydrovolcanism: basic considerations and review. *J. Volcanol. Geotherm. Res.*, 17: 1–29.
- Smith, R.L., 1979. Ash-flow magmatism. *Geol. Soc. Am. Spec. Pap.*, 180: 5–27.
- Sparks, R.S.J., 1978. The dynamics of bubble formation and growth in magmas: a review and analysts. *J. Volcanol. Geotherm. Res.*, 3: 1–37.
- Sparks, R.S.J. and Brazier, S., 1982. New evidence for degassing processes during explosive eruptions. *Nature*, 295: 21–23.
- Stuiver, M. and Pearson, G.W., 1986. High-precision calibration of the radiocarbon time scale, AD 1950–500 BC. In: M. Stuiver and R.S. Kra (Editors), *Int. ¹⁴C Conf.*, 12th, *Proc. Radiocarbon*, 28 (2B): 805–838.
- Stuiver, M. and Polach, H.A., 1977. Discussion: reporting on ¹⁴C data. *Radiocarbon*, 19: 355–363.
- Stuiver, M. and Reimer, P.J., 1986. A computer program for radiocarbon age calibration. *Radiocarbon*, 28: 1022–1030.
- Verhoogen, J., 1951. Mechanisms of volcanic ash formation. *Am. J. Sci.*, 249: 29–39.
- Vezzoli, L. (Editor), 1988. *Island of Ischia*. CNR, Quaderni de "La Ricerca Scientifica", 114, 10, 122 pp.
- Vogel, J.S., Southon, J.R., Nelson, D.E. and Brown, T.A., 1984. Performance of catalytically condensed carbon for use in accelerator mass spectrometry. *Nucl. Instrum. Methods Phys. Res.*, B5: 289–293.
- Vogel, J.S., Southon, J.R. and Nelson D.E., 1987. Catalyst and binder effects in the use of filamentous graphite for AMS. *Nucl. Instrum. Methods Phys. Res.*, B29: 50–56.
- Walker, G.P.L., 1971. Grain-size characteristics of pyroclastic deposits. *J. Geol.*, 79: 696–714.
- Whitham, A.G. and Sparks, R.S.J., 1986. Pumice. *Bull. Volcanol.*, 48: 209–224.
- Wohletz, K.H. and Sheridan, M.F., 1979. A model of pyroclastic surge. *Geol. Soc. Am. Spec. Pap.*, 180: 177–193.
- Wohletz, K.H., Sheridan, M.F. and Brown, W.K., 1989. Particle size distributions and the sequential fragmentation/transport theory applied to volcanic ash. *J. Geophys. Res.*, 94 (B11): 15,703–15,721.